Research paper

Study of the Dynamic Processes of Multi-point Initiation of Co-axial Explosively Formed Projectiles with Tail Wings Using High Speed Image Processing Technologies

Chang-Xiao Zhao[1], **Yangfan Cheng**[2,*], **Dan-Yi Li**[2],
Bei-Bei Zhang[2], **Xin Wang**[1], **Chong Ji**[1]

[1] *School of Field Engineering, Army Engineering University of PLA, China*

[2] *School of Chemical Engineering, Anhui University of Science and Technology, China*

* E-mail: yfcheng208@163.com

Abstract: In order to study the dynamic processes of co-axial explosively formed projectiles (CEFP) with tail wings formed by multi-point initiation, a novel image processing technique based on a high-speed camera was designed. The temperature field distribution and formation process of a CEFP with tail wings, formed by multi-point initiation, can be measured using the colorimetric temperature measurement method, the binary image processing technique, and contour detection technologies. The experimental results were verified using LS-DYNA software. The experimental results showed that a projectile with a regular shape and four symmetrical tail wings was formed by initiating the shaped charge with a double-layer liner at four points. The explosion temperature of the detonation products was in the range of 2000-2600 K, and the explosion pressure at the detonation center was 6.92 GPa. The morphology, flight velocity, and draw ratio of the CEFP obtained using the high-speed image processing technology were in good agreement with numerical simulation results, which demonstrates a promising application prospect for measuring the explosion temperature, flight velocity, and motion attitude of shells, rockets, and other kinds of weapons.

Keywords: explosively-formed projectile, multi-point initiation, shaped charge, hollow charge, tail wing, high-speed image

1   Introduction

With the rapid development of damage technology and defense technology, the lethality of weapons and equipment has an increasing impact on the battlefield, which makes weapon damage efficiency and armour defense performance hot issues of the military research . The explosively formed projectile (EFP) has the characteristics of strong anti-interference capability as well as an outstanding penetration effect, and the behind armour debris could strike targets such as armour and tanks, which could effectively destroy targets and improve combat effectiveness [1-4]. A coaxial explosively formed projectile (CEFP) warhead is a shaped charge warhead based on a single EFP warhead which is designed with a multi-layer liner structure. Compared with the traditional EFP warhead, a CEFP warhead could form several coaxial projectiles with the same energies, has and have a physical structure of front and rear separation. The front projectile may be used to initiate explosive reactive armour, while the rear projectile could continue to penetrate the main armour, the combination of the two projectiles effectively improving the damage ability and damage efficiency against the explosive reactive armour targets [5, 6].

However, it was found that front-rear separation projectiles will overturn during flight due to poor aerodynamic performance [5], and would not hit the target accurately from a long distance. Therefore, to avoid the tumbling phenomenon of the projectiles during flight, it is required that the projectiles should have a good aerodynamically stable shape. Previous studies [7-9] have found that multi-point initiation could make a single EFP tail form multiple symmetrically distributed fin tail wings, thus effectively improving the aerodynamic characteristics of the EFP and reducing the angle of attack and flying resistance between the projectile and the target, and thus improving the target landing accuracy. Weimann [10] studied the effects of charge parameters and liner structures on the formation and flight stability of EFPs, and proposed the idea of forming EFPs with tail wings by multi-point initiation. Liu *et al.* [11] generated EFPs with fins by three-point initiation, which could significantly reduce the flight resistance of an EFP and improve its aerodynamic stability. Li *et al.* [12] studied the effects of multi-point initiation modes on the velocity and aspect ratio length (L) to diameter (d), *i.e.* L/d of an EFP, by numerical simulation. The results showed that the velocity of an EFP had a linear relationship with the initiation radius of the EFP, and the aspect ratio had a hyperbolic relationship with the initiation radius of the EFP.

The penetration and damage performance of EFPs are not only related to the velocity and draw ratio of the projectile, but are also related to the molding structure and flying state of the projectile. Therefore, it is of great importance to

capture the molding structures and flying processes of EFP. Li *et al.* [13] collected EFP projectiles through a recovery device (cylinder with foam and wood flour); the shape of the EFPs collected by this method were seriously damaged, and the flight process of the projectiles could not be observed. Liu *et al.* [14] measured the velocity, penetration ability, and molding processes of EFPs by pulsed X-ray photography, and the experimental results were in good agreement with simulation results. Ma *et al.* [15] measured the formation and separation of tandem EFPs by pulsed X-ray photography and divided them into an impact phase, a propulsion phase, a slide phase, and a free flight phase. Pulsed X-ray photography has strong penetrating ability and could monitor the formation process of an EFP, but X-ray has the disadvantages of a small measurement range, low spatial resolution, and high cost, and only takes one frame of a transient response, so it is impossible to realize the study of the whole forming process. In recent years, with the rapid development of high-speed camera technology, high-speed cameras have been widely used in trajectory tracking, missile launching, combustion tests, material tests, particle image velocimetry (PIV) tests and other fields. The colorimetric temperature measurement technology used in the present study is based on a high-speed camera, and could reconstruct the dynamic temperature distribution in the transient explosion processes. As a non-contact temperature measurement method, the colorimetric temperature measurement method does not need to obtain the emissivity of the measured object, and has incomparable advantages over the infrared thermal imaging temperature measurement method [16]. In addition, with its high-frequency shooting speed, the high-speed camera has the ability to capture the moving trajectory of high-speed objects that ordinary cameras could not, accurately tracking the movement of objects, and measuring their morphology, size, distance change, and moving speed. In addition, the high speed image processing technologies based on the colorimetric temperature measurement method have the advantages of easy-capture and low-cost, and is significantly better than the recovery device, pulse X-ray photography and other methods. It can accurately capture the temperature field distribution, molding structure and flight state in the forming process of an EFP [17, 18], providing support for the subsequent improvement in design of EFPs.

In order to study the dynamic processes of an EFP with tail wings formed by multi-point initiation, the temperature field distribution and formation processes of a CEFP with tail wings formed by multi-point initiation were systematically studied using the colorimetric temperature measurement method, binary image processing technology, and gauze target experiments. At the same time, the forming processes of a CEFP with tail wings formed by multi-point initiation was numerically simulated by the LS-DYNA software, and the results were

compared with the experimental results. The image processing technology based on the high-speed camera could measure the explosion temperature distribution, morphology, and flight velocity of a CEFP during its formation process. It has the characteristics of being intuitive and reliable, as well as giving high measurement accuracy, which provides a novel test method for the CEFP forming process and flight attitude capture.

2   Materials and Methods

2.1 Structural parameters of the shaped charges

The main charge was a 572 g paraffin passivated RDX column with a cavity (provided by Anhui Wanhuai Electromechanical Co., Ltd.), and with charge diameter, L, 100 mm, charge height (H) 50 mm and charge density (ρ) 1.65 g/cm³. The bottom of the shape charge was composed of two red copper liners (one with a variable wall thickness and the other one with a uniform wall thickness). The outer radius (R_0) and inner radius (R_i) of the inner liner with variable wall thickness were 104 and 80 mm, respectively, while the outer and inner radii (R_r) of the outer liner with uniform wall thickness were both 80 mm, and the wall thickness was 2 mm, as shown in Figure 1(a). Figure 1(b) shows the physical image of the shaped charge with a double-layer liner, which were an uniform wall thickness liner, a variable wall thickness liner and an RDX column from top to bottom, respectively.
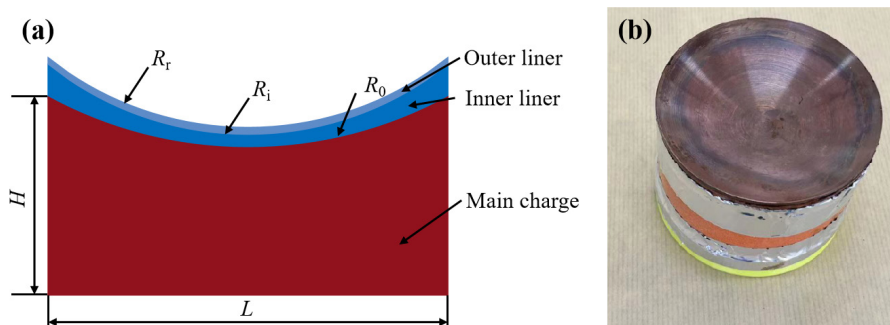

Figure 1.   Shaped charge with double-layer liner (a) structure chart and (b) actual product image

2.2 Experimental facilities and methods

In the experiments, the flight attitude (the shape of tail wing) of the CEEP was recorded by gauze and paperboard, as shown in Figure 2(a), and the CEEP

forming processes were captured using a high-speed camera. The RDX column was initiated by detonating four detonating cords using a detonator for four-point synchronous triggering (the detonation radius was 20 mm). The shaped charge was composed of four detonating cords, a cap (containing four symmetrical holes), an RDX column with a cavity, liners with variable wall thickness, and uniform wall thickness, as shown in Figure 2(b). In the experiments, the high-speed camera and the PCB shock wave pressure sensor were placed at distances of 30 and 5 m from the charge, respectively, the shaped charge was 5 m from the first target, and the distance between each adjacent target was also 5 m.
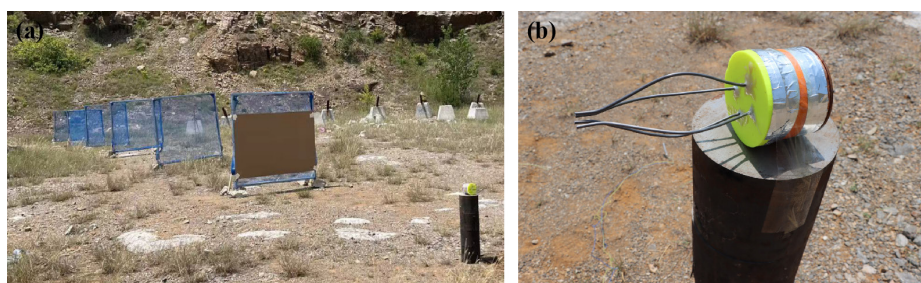

Figure 2. Recording the flight attitude of the CEEP: (a) experimental setup and (b) shaped charge with four initiating points

3   Numerical Simulation

3.1 Establishment of the model

In order to analyze the influence of a multi-point initiation mode on the explosive formation of a CEFP, the dynamic processes were simulated by LS-DYNA software, as shown in Figure 3. The shaped charge was composed of an RDX column, two liners with a variable wall thickness and a uniform wall thickness, and all parts of the shaped charge were modelled by an eight-node hexahedral element in equal proportions according to the object. The shaped charge was initiated by four symmetrical initiation points on the end face of the explosive. An Arbitrary Lagrangian Eulerian (ALE) was used to reproduce the RDX behaviour in LS-DYNA, while for both liners a Lagrangian description was used, since it could clearly depict the relative motions between different interfaces when compared with Euler algorithm, facilitating the determination of physical quantities at specific points.
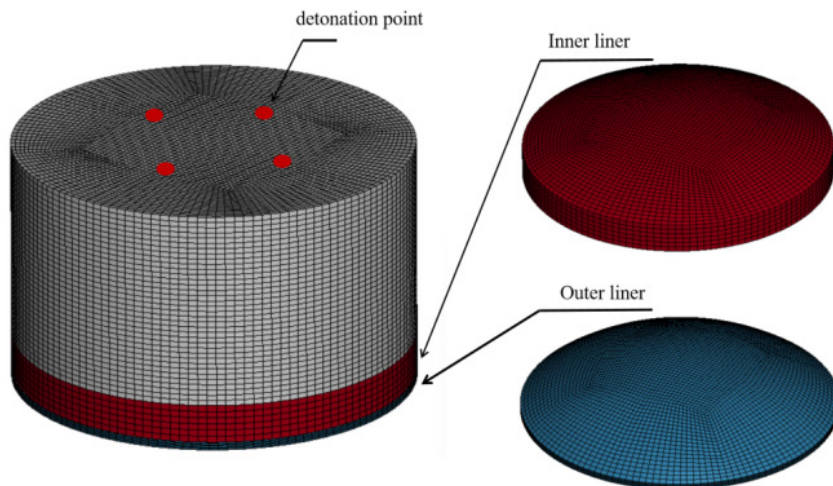
Figure 3. Finite element model of multi-point initiated shaped charge with double-layer liner

3.2 Material model parameters

The state equation of the detonation products is to describe the relationships between physical quantities such as pressure, internal energy, and volume after detonation reaches the C-J state. RDX was described by the high explosive material model of MAT_HIGH_EXPLOSIVE_BURN and the EOS_JWL state equation shown in Equation 1.

$$P = A\left(1 - \frac{\omega}{R_1 V}\right)e^{-R_1 V} + B\left(1 - \frac{\omega}{R_2 V}\right)e^{-R_2 V} + \frac{\omega E}{V} \tag{1}$$

where P represents the pressure of the detonation products, V represents the relative specific volume, E represents the specific internal energy. The symbols of A, B, R_1, R_2, ω are constants. The specific parameters of the explosive are listed in Table 1.

Table 1. Material model parameters of RDX

ρ [g/cm³]	D [m/s]	P_{CJ} [GPa]	A [GPa]	B [GPa]	R_1	R_2	ω
1.65	7740	28	371.2	3.21	4.15	0.95	0.3

The double-layer liner was made of copper, which was described by the MAT_JOHNSON_COOK constitutive model and the EOS_GRUNEISEN state

equation [19]. The Johnson-Cook constitutive model could reflect the strain rate strengthening effect and temperature rise softening effect of the ideal steel plastic strengthening model, which is widely used to describe the mechanical properties of metallic materials under explosive loading, and the copper material model can be described in Equation 2.

$$\sigma_y = \left(A + B\bar{\varepsilon}^{p^n}\right)\left(1 + c\ln\dot{\varepsilon}^*\right)\left(1 - T^{*m}\right) \tag{2}$$

where $\bar{\varepsilon}^p$ is the normalized equivalent plastic strain, $\dot{\varepsilon}^*$ is the normalized equivalent plastic strain rate. The symbols of A, B, c, m and n are the material constants. T^* represents the relative temperature and can be calculated with the following equation:

$$T^* = \frac{T - T_{room}}{T_{melt} - T_{room}} \tag{3}$$

where T, T_{melt}, and T_{room} are the absolute, melting, and room temperatures, respectively.

The Gruneisen equation of state with cubic shock-velocity as a function of particle-velocity defines pressure for compressed materials as follows:

$$P = \frac{\rho_0 C^2 \mu \left[1 + \left(1 - \frac{\gamma_0}{2}\right)\mu - \frac{a}{2}\mu^2\right]}{\left[1 - (S_1 - 1)\mu - S_2\frac{\mu^2}{\mu+1} - S_3\frac{\mu^3}{(\mu+1)^2}\right]^2} + (\gamma_0 + a\mu)E \tag{4}$$

and for expanded materials as follows:

$$P = \rho_0 C^2 \mu + (\gamma_0 + a\mu)E \tag{5}$$

where P is pressure, C is the intercept of the v_s-v_p curve, S is the coefficient of the slope of the v_s-v_p curve, γ_0 represents the Gruneisen coefficient and a is the first-order volume correction coefficient of γ_0. The relative compressibility is $\mu = \rho/\rho_0 - 1$, in which ρ_0 is the initial density of the material, and E is the initial internal energy. The material model parameters of the liners are listed in Table 2.

Table 2.   Material model parameters of the liners [20]

ρ [g/cm^3]	E [GPa]	A [MPa]	B [MPa]	n	C	m	T_r [K]
8.968	117.2	9	292	0.31	0.025	1.09	293

3.3 Mesh convergence analysis

The LS-DYNA finite element software was used to simulate the forming process of the explosively formed projectile. Firstly, the convergence analysis of the mesh size was needed to determine a reasonable mesh size for the numerical model. Therefore, four groups of models with mesh elements of 21312, 83520, 176424 and 334080 were established for numerical simulation of EFP molding. Figure 4 shows the velocity-time curves of the inner and outer liners within 400 µs under different mesh sizes. In the first group of models, due to the large mesh size, the mesh elements were distorted, so the calculation could not be carried out normally, and no data were obtained.
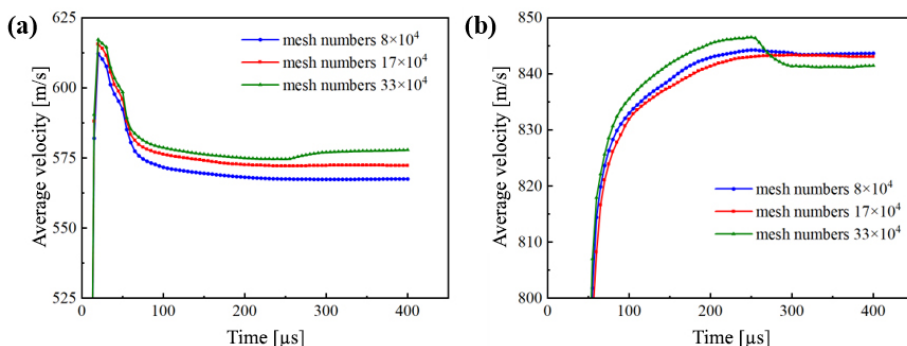
Figure 4.   Average velocity-time curves of the inner liner (a) and the outer liner (b)

Figure 4 shows that as the mesh size is increased, the average velocity of the inner liner gradually increases, but in the model with 334080 mesh elements, there is a sudden rise in velocity. The average velocity of the outer liner increased with the increase in mesh number, but there was also a sudden drop in velocity with the precise mesh size [21]. Comparing the average velocity-time curves of the two liners with different mesh sizes, it could be considered that the numerical simulation with grid elements in the range of 80,000-170,000 was convergent. Therefore, in order to ensure the convergence and calculation accuracy of the numerical simulation, and to avoid unnecessary numerical simulation calculation time, 170,000 mesh elements were selected for the subsequent numerical simulation research.

4   Results and Discussion

4.1 Witness experiments for tail shapes of the CEFPs

In the physical experiments, the integrity, morphology, and flight stability of the CEFPs were judged by the hole pattern left on the gauze target after the CEFP had passed through. Figure 5 shows that there was a hole with four wings on the gauze target, which certificated that the multi-point detonation of a shaped charge with a double-layer liner would form a CEFP with four symmetrical tail wings and good flight stability during the penetration [22].

Figure 5.   Hole pattern left on the gauze target after the CEFP had passed through

4.2 Detonation parameters during the formation processes of a CEFP

In the formation process of an EFP, the temperature distribution fields and shock wave parameters are two crucial parameters, which have a significant impact on the formation performance and the final penetration performance of the EFP. Therefore, it is necessary to measure the temperature distribution fields and shock wave parameters during the explosion.

4.2.1 Temperature distribution

The colorimetric temperature measurement method is based on the blackbody radiation law, and the dynamic distribution of the RDX explosion temperature field during the formation of the CEFP in this study was reconstructed by high-speed images. The image sensor of a CMOS high-speed camera is composed

of a single point sensor array, which adopts the Bayer array of GRBG mode, as shown in Figure 6.

Figure 6.   Bayer array of the high-speed camera, where R means red, G means green and B means blue

Each single point sensor corresponds to a certain colour component of R, G or B component, and R, G and B correspond to different optical bands, respectively. The single value function of temperature could be obtained by calculating the ratio of signals in different bands as follows:

$$T = \frac{c_2 \left(\dfrac{1}{\lambda_2} - \dfrac{1}{\lambda_1} \right)}{\ln K - \ln \left[\dfrac{\varepsilon(\lambda_1, T)}{\varepsilon(\lambda_2, T)} \right] - 5 \ln \left(\dfrac{\lambda_2}{\lambda_1} \right)} \tag{5}$$

where T is the thermodynamic temperature, λ is the wavelength, c_2 is the Planck's second radiation constant, $\varepsilon(\lambda_i, T)$ is the emissivity of the object at the wavelength λ_i, and K is the ratio of radiation luminance at two wavelengths λ_1 and λ_2 of the blackbody at temperature T.

Before the experiments, it is necessary to carry out a temperature measurement calibration of the system. The calibration system consisted of

a circuit with a tungsten lamp and a high-speed camera, as shown in Figure 7(a). The high-speed camera was used to record the gray images of the tungsten filament lamp under different currents, the R/G value was calculated by the interpolation algorithm. The temperature of the tungsten filament lamp was calculated from the ratio of the resistance R_A of the tungsten filament lamp under different currents to its initial resistance R_0 [23]. The temperature calibration curve is shown in Figure 7(b).
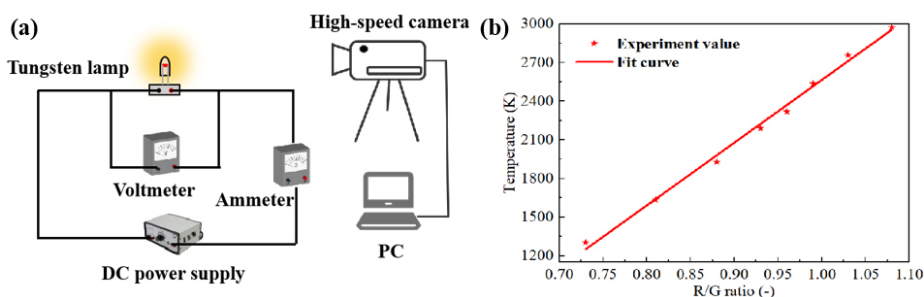
Figure 7. Temperature calibration experiment: Calibration system (a) and calibration fitting curve (b)

Figure 8 shows the gray images of the explosion processes of the CEFP with tail wings in the time range of 0-646.8 µs, and the detonation moment was defined as $t = 0$. After the initiation of the shaped charge, the explosion products diffused outwards and exchanged heat with the external environment. The explosion fireball kept growing and doing work externally through compressing the ambient air. The energy was dissipated to the surrounding environment in the forms of a shock wave, heat, light, and sound during the whole detonation processes until the explosion fireball became extinguished [24, 25]. Figure 8 shows that the RDX column exploded during 0 to 58.8 µs; when t was in the range of 58.8-176.4 µs, there was an obvious sharp corner in the explosion flame front, which was attributed to the detonation wave begining to crush the double-layer liner to form the CEFP; when t was between 176.4 and 352.8 µs, the detonation flame continued to propagate forwards and the formation of the CEFP was gradually completed. Furthermore, when t was in the range of 352.8-646.8 µs, the explosion gas exchanged heat with the external environment, and the explosion flame became gradually extinguished. When $t = 646.8$ µs, the CEFP had been formed and moved forward at a certain speed, and the shape of the formed projectile with tail wings could be clearly observed.

Based on the gray images of the detonation processes of the shaped charge presented in Figure 8, the detonation temperature distributions at different times
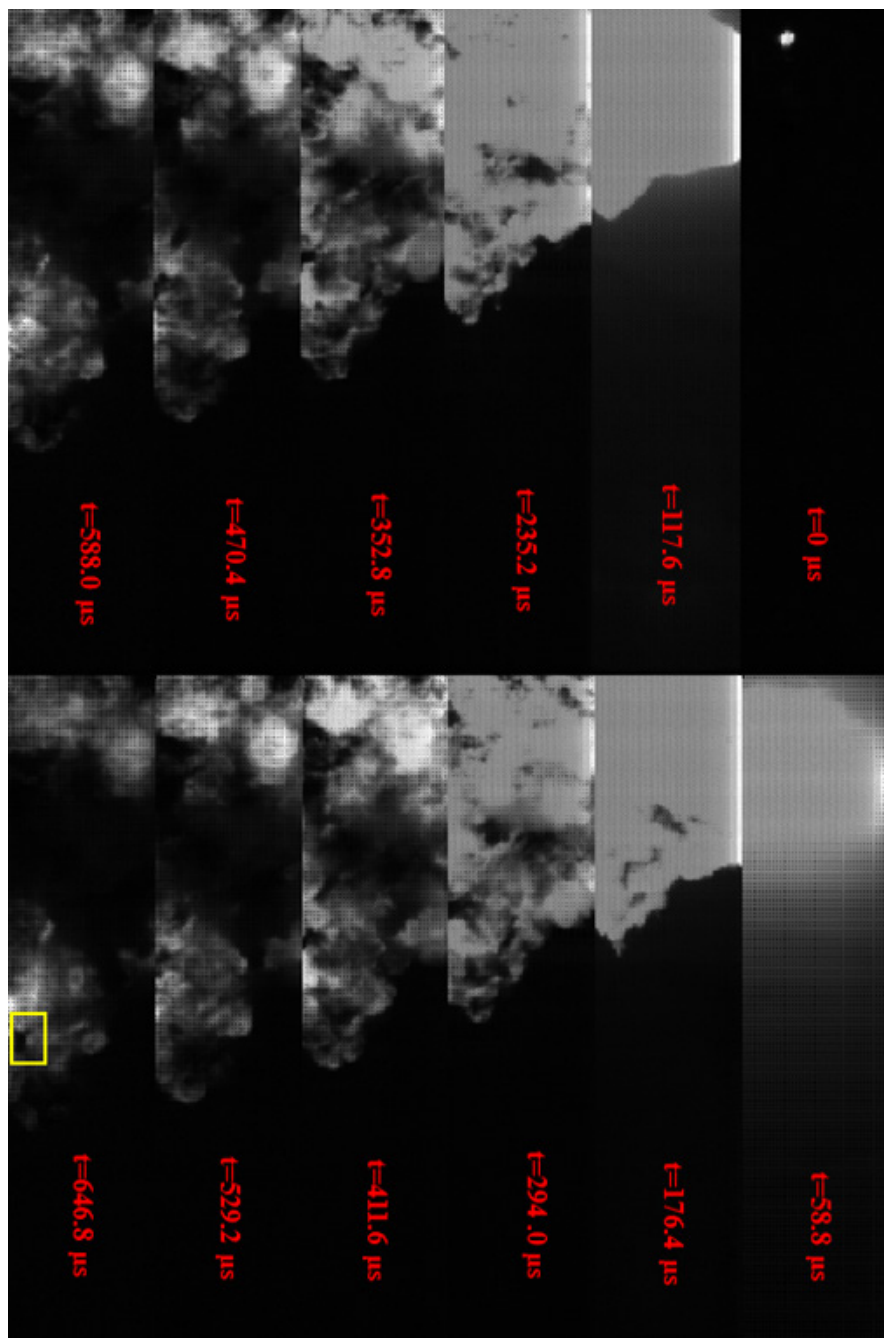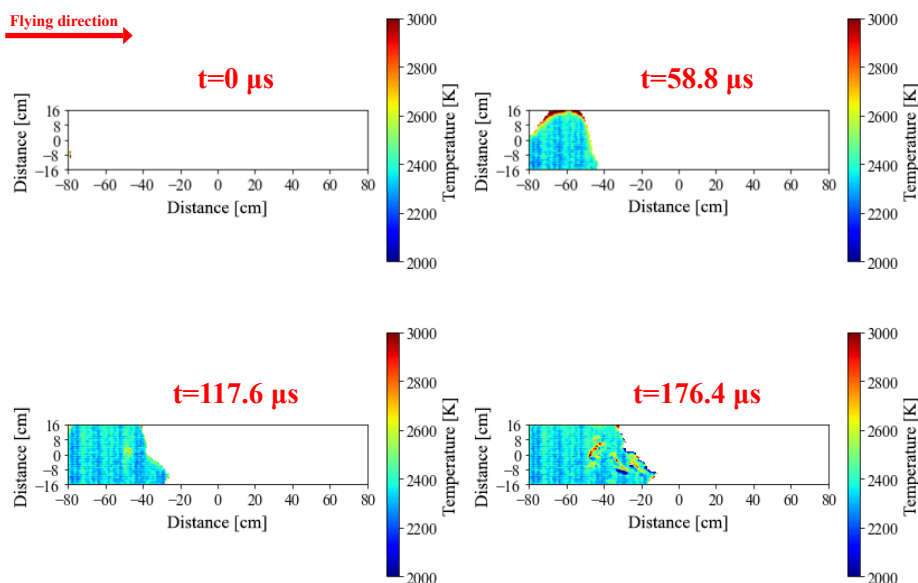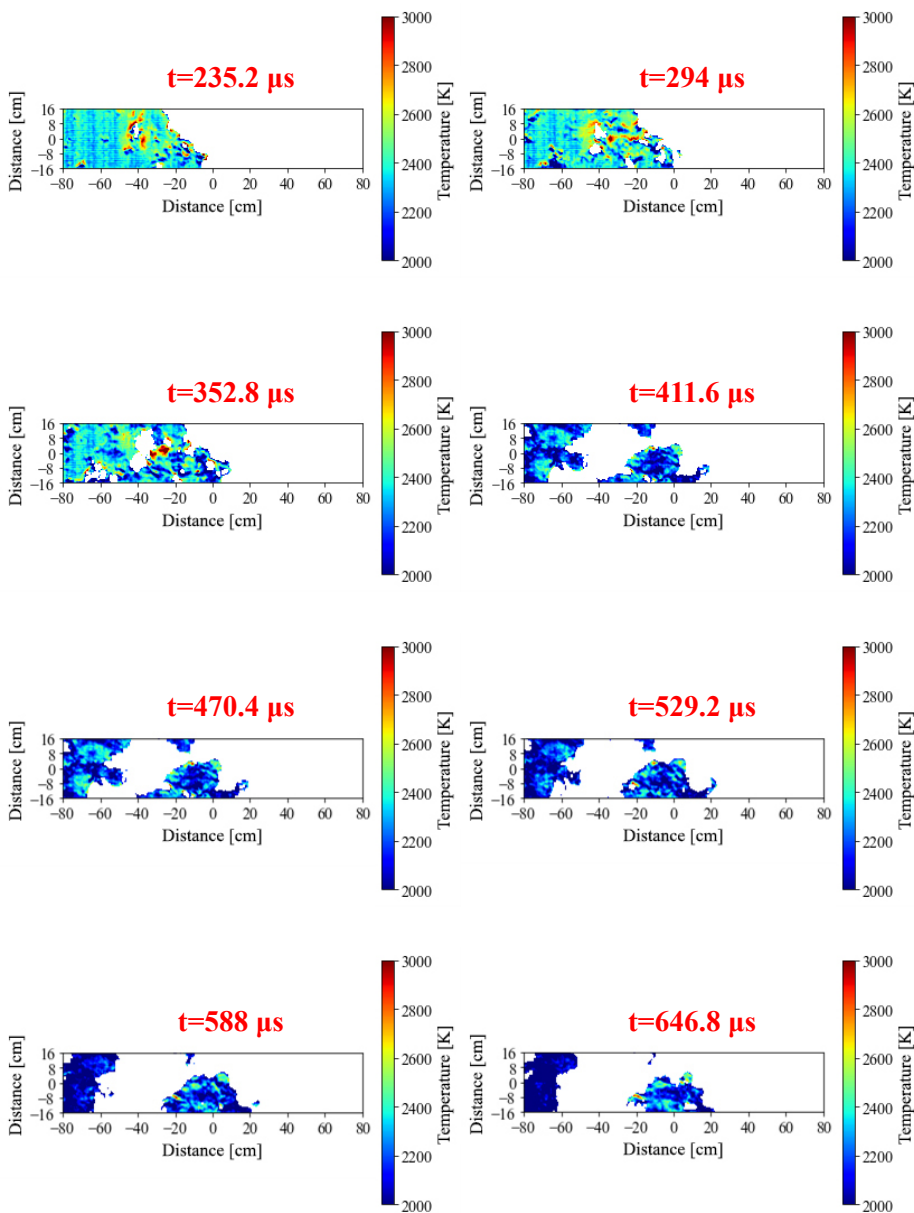
Figure 8. Gray images of the explosion process of a double-layer CEFP warhead with tail wings

were calculated using colorimetric temperature measurement technology, as shown in Figure 9. At $t = 0$-352.8 μs, the temperature of the detonation product was in the range of 2300-2600 K, and at the moment of $t = 58.8$ μs, the upper edge zone temperatures of the explosive gaseous products were higher than the internal zone. In the time range of t from 352.8 to 646.8 μs, the temperature of the detonation products decreased continuously and was distributed in the range of 2000-2300 K. When t was between 529.2 and 646.8 μs, the temperatures of the detonation products at the initiation point of the shaped charge were lower than those around the CEFP, because after detonation of the shaped charge, the explosive fireball continued to spread forwards. The overall temperature of the explosive products represented a slow decline, while the CEFP had a higher temperature in the formation processes and would thus heat up the surrounding gases. Consequently, the temperature field attenuation of the gases around the CEFP was slower than that of the gases at the initiation position.

Figure 9.   Temperature field distributions during the explosion processes of the shaped charge

4.2.2 Shock wave pressure

The mass of RDX used in the experiments was 572 g, and the distance between the PCB pressure sensor and the center of the shaped charge was 5 m. Figure 10 shows the experimental and numerical simulation results of the shock wave pressure-time curves for 572 g RDX measured at 5 m away from the charge center. Their shock wave peak pressures were very close, so the experimental value of the detonation pressure in the centre of the shaped charge could be reversed via numerical simulation, and the value was *ca.* 6.92 GPa.

From the above analysis, we can draw the conclusion that the double-layer liner formed the CEFP under temperatures of 2300-2600 K and a pressure of 6.92 GPa created by the RDX detonation.
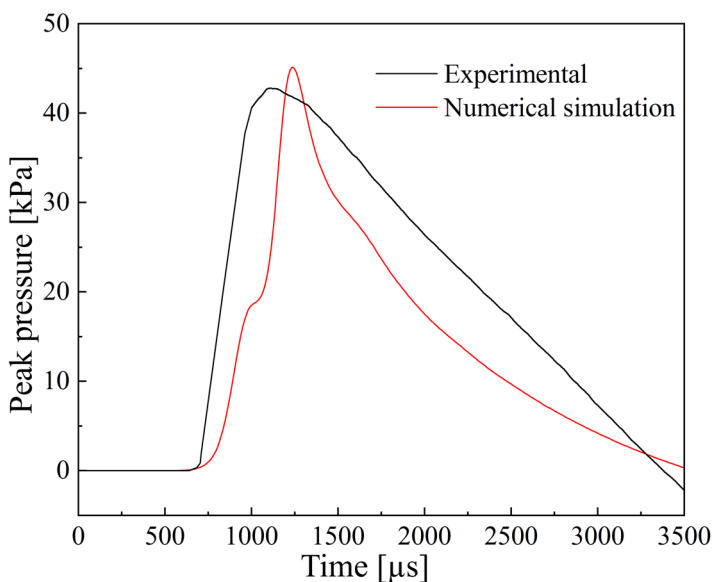
Figure 10. Experimental and numerical results of the shock wave pressure-time curves for RDX

4.3 Flight processes of a CEFP

Figure 11 shows high-speed images of the formation processes of the CEFP. In order to better obtain the characteristic parameters of the CEFP, the original images were transformed into gray-scale images and binary processing was performed. Image binarization is the process of setting the pixel value of an image to be 0 or 255, as follows:

$$binary(x, y) = \begin{cases} 255, \ gray(x, y) > threshold \\ 0, \ gray(x, y) \leq threshold \end{cases} \tag{6}$$

where $gray(x, y)$ presents the pixel value of a gray-level image in the row x and column y, *threshold* is set manually and $binary(x, y)$ presents the binarized pixel value. The pixel value of the gray image is set to be 255 when its value is greater than the *threshold*, otherwise it is set 0; finally a black-and-white binarized image will be obtained. Figures 11(a) and (b) show the effect of converting an image of the CEFP flight process into a binarized one.

Figure 11. Process of high-speed photographic image: (a) original image and (b) binarized image

As indicated in Figure 11(b), the flame was white and the CEFP was black after binarization. Consequently, it became easier and more accurate for the detection of the CEFP. The the image was then processed by the edge detection algorithm to obtain a minimum boundary rectangular frame that could encapsulate it, as shown in Figure 12. OpenCV of the Python software provides a method that takes an outline as an input parameter and takes the coordinates of the smallest rectangular box containing that outline as an output. Thus the coordinates (x, y) of the upper lefthand corner of the rectangle, the height h and the width w of the rectangle were obtained, and the other three coordinates of the contours could be obtained by means of x, y, w and h.

**Figure 12.** Minimum rectangular frame

However, it should be noted that the coordinates calculated by the code were the pixel units of the contour in the image. Therefore, in order to get their true lengths, a calibration experiment should be carried out. As shown in Figure 13, a light-emitting cube was selected as a reference object in the calibration experiment. The true side length (L_t) of the cube could be measured; furthermore, the shooting distance and focal length were kept the same in the calibration experiment and in the detonation experiment. The edge detection and contour area calculation of the calibration object were performed, and its pixel edge length (L_p) was obtained. The calibration coefficient k was expressed by the ratio of the real side length L_t and the pixel side length L_p of the calibration object, as follows:

$$k = \frac{L_t}{L_p} \tag{7}$$

The calibration coefficient of pixel length and its real length was obtained from the length-scale calibration experiment, and the flight velocity of the CEFP was calculated.
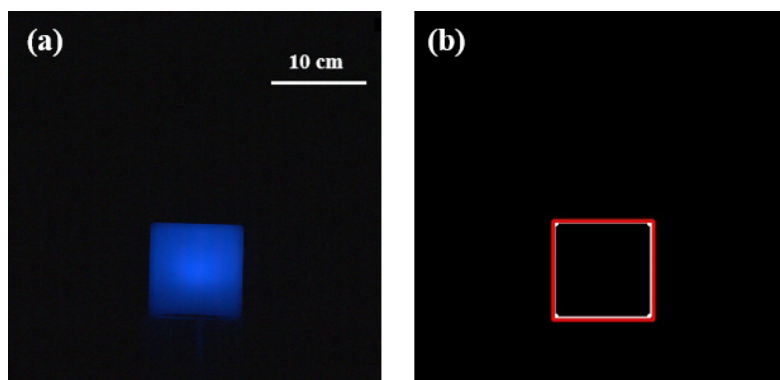

Figure 13. Proportional length calibration experiment: real product image (a) and contour detection chart (b)
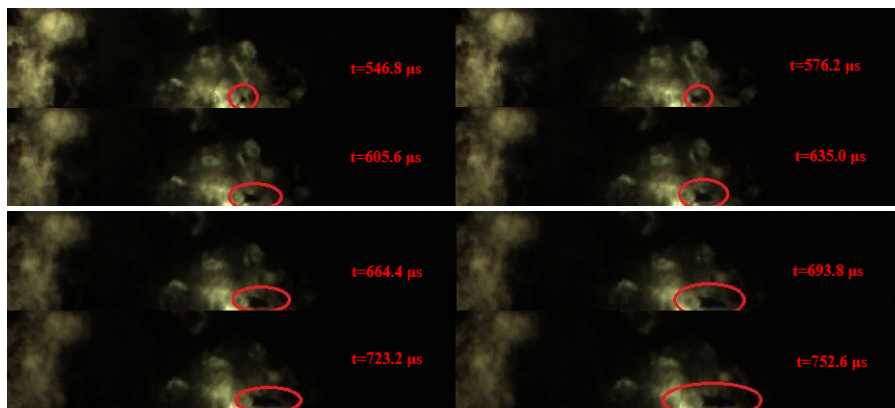
Figure 14. High-speed images of the formation process of a CEFP with tail wings

Figure 14 clearly shows that a CEFP with tail wings could be formed after multi-point initiation of the double-layer liner. Based on the binarization method, the contour detection technique and the calibration coefficient for the high-speed images, the curves for the head displacement and the flight velocity of the CEFP (unseparated) over time were obtained. As shown in Figure 15, the average flight velocity of the CEFP was 1041 m/s.
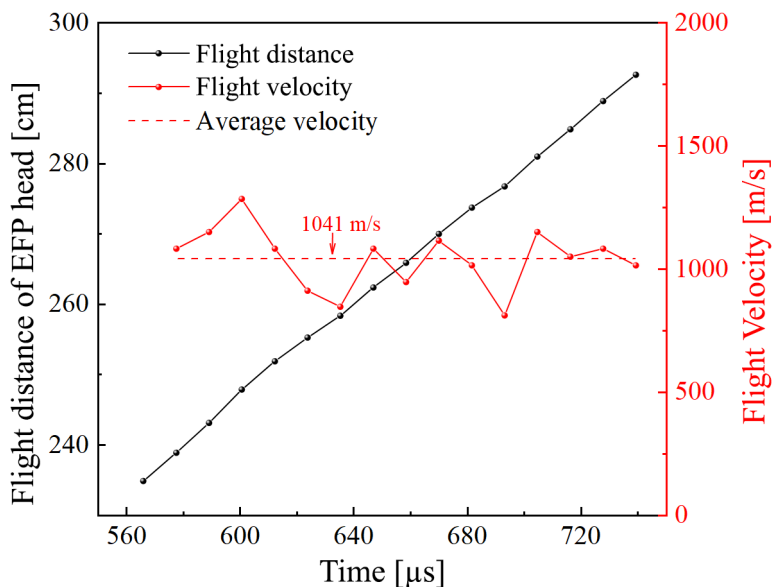
Figure 15. Time-dependent curves of the head displacement and flight velocity of the CEFP

4.4 Characteristic parameters of the CEFP during its formation processes

4.4.1 Multi-point initiation to form a CEFP with tail wings
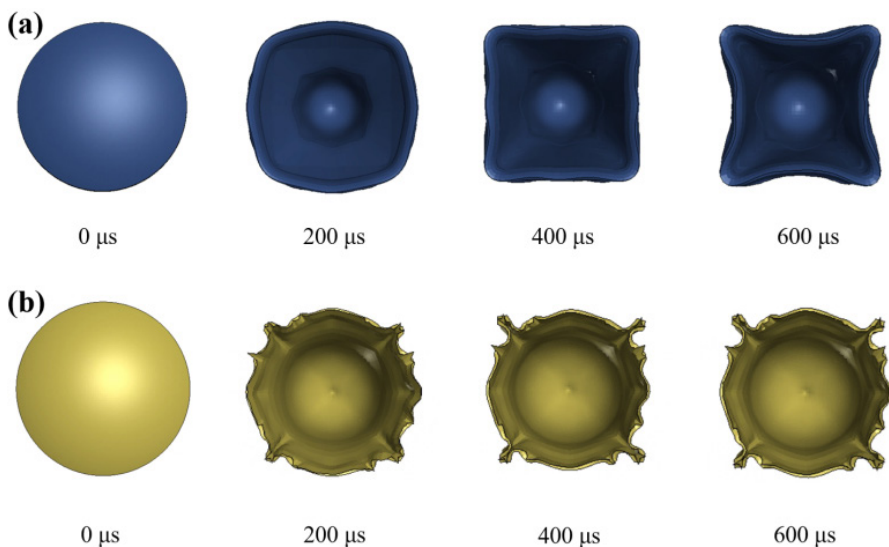
Figure 16. Dynamic deformation of a double-layer liner with multi-point initiation: inner liner (a) and outer liner (b)

Figure 16 shows the formation processes of a CEFP with tail wings by initiating the double-layer liner at multiple points. When the explosive was detonated at multiple points, the detonation wave produced by each initiation point propagated in the form of a spherical wave. The detonation waves at the adjacent positions would meet at their symmetrical surface and collide violently as they propagated continuously, forming a Mach wave. The shock wave collision caused stress concentration and overpressure in the symmetric plane of two adjacent detonation points. The pressure on the micro-element in contact with the Mach wave was higher than that in the non-Mach region, and the pressure on the liner decreased with increasing distance from the Mach region. Because the pressure gradient on the liner surface changed, the liner turned over asynchronously, and symmetrical and uniform protrusions were formed at the end of the CEFP, producing a projectile with four symmetrical tail wings, which was consistent with the morphology of the CEFP obtained by the gauze target experiments. Furthermore, Figure 16 also shows that the dynamic
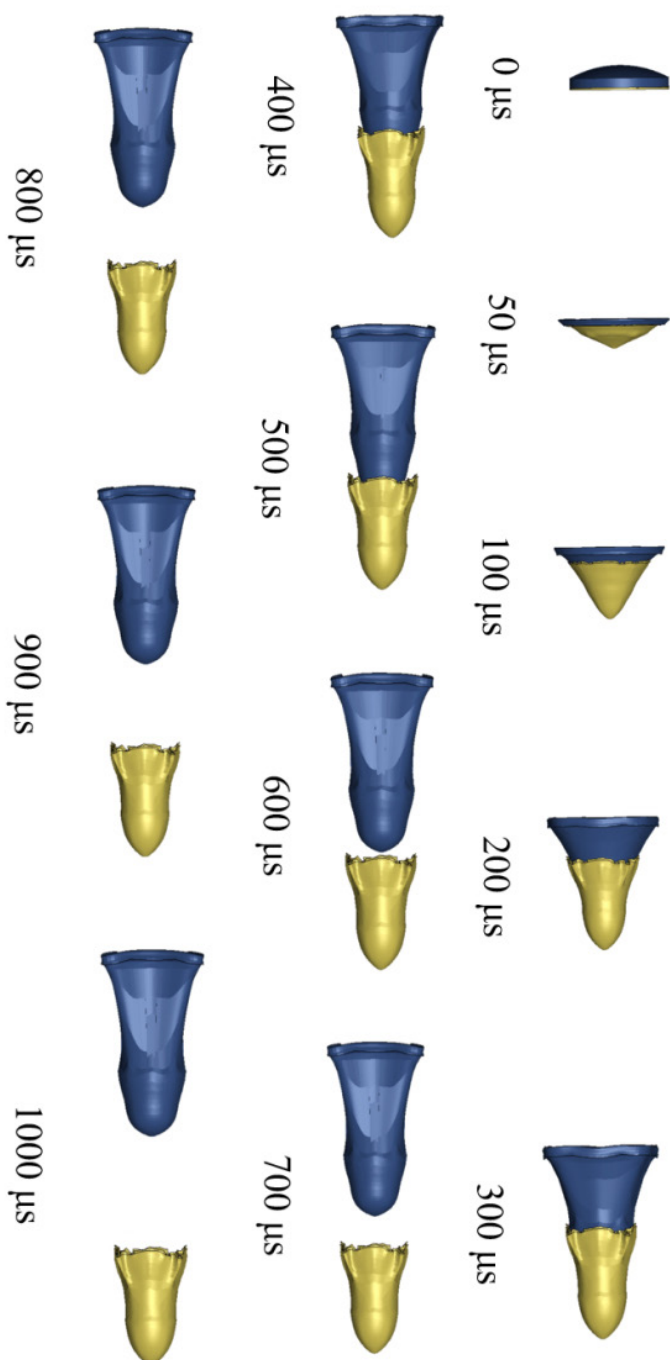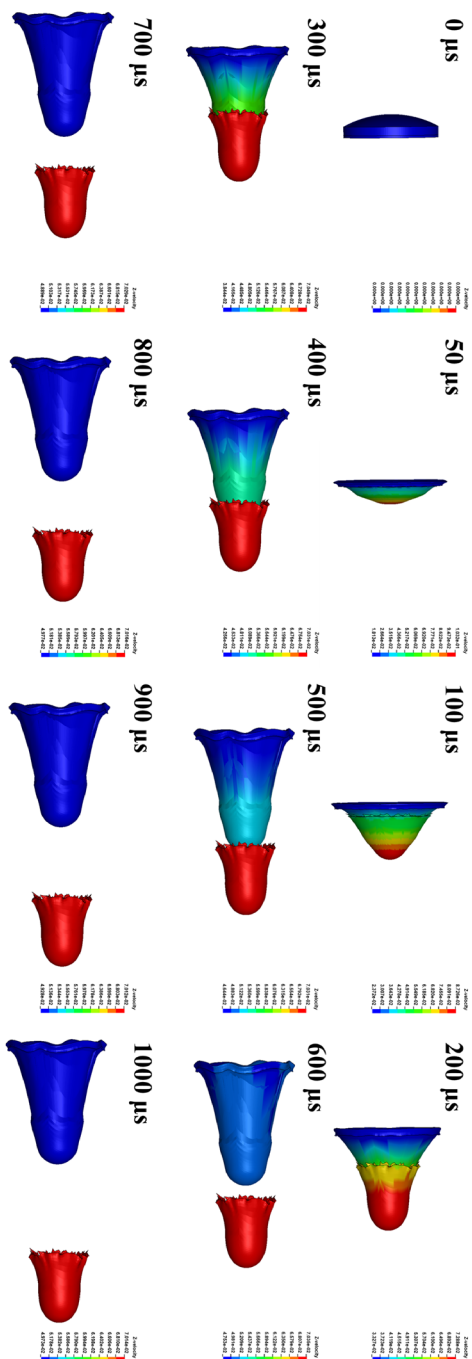
Figure 17. Dynamic formation processes of a four-point initiated CEFP

response of the outer liner lagged behind than that of the inner liner, because the axially propagated shock wave passed through the inner liner to impact the outer liner, and the shock wave energy acting on the outer liner was less than that on the inner liner.

4.4.2 Formation and separation processes of a CEFP

The formation processes of a CEFP based on the double-layer liner were crucial for the study of the formation mechanism of the CEFP. Through LS-DYNA numerical simulation, the formation and separation processes of the CEFP by four-point initiation of the double-layer liner were simulated, and the results are shown in Figure 17.

The formation process could be divided into three phases, the impact phase, the propulsion phase and the free flight phase [15]. In the formation process of a CEFP, there was a free surface between the double-layer liners, and they would collide and slide with each other under the joint impact acceleration of the shock wave and the detonation products. In Figure 17, the initial moment of CEFP formation was set as $t = 0$ s. The impact phase of the double-layer liner was in the time range of $t = 0$-100 µs. The shock wave initially acted on the inner liner to obtain the initial axial velocity, and a reflection stretch wave was formed when the shock wave reached the free interface and would be reflected. The outer liner was also accelerated under the joint action of the transmission shock wave and the reflected stretch wave, because of which the inner and outer liners collided with each other and a gap would be produced. Subsequently, due to the acceleration effect caused by the high temperature and high pressure detonation products, the inner liner caught up with the outer liner and collided again, and this process was then repeated until the detonation product could not accelerate the inner liner any more. In the time range of $t = 100$-500 µs, the double-layer liner was in the propulsion phase, where the shock wave first acts on the top part of the liner and the projectile head was formed. At this time, the axial velocity of the top of the liner was higher than that of the bottom part, and the liner flipped back to form an irregularly shaped CEFP with four symmetrical tail wings. Subsequently, the CEFP gradually separated due to the speed differences of the two projectiles. In the time range of $t = 500$-900 µs, the CEFP was in the free flight phase, and its two projectiles were not in contact with each other anymore, forming a double-layer series CEFP with stable draw ratios and flight velocity.

Figure 18. Velocity distribution field of the dynamic formation processes of a four-point initiated CEFP
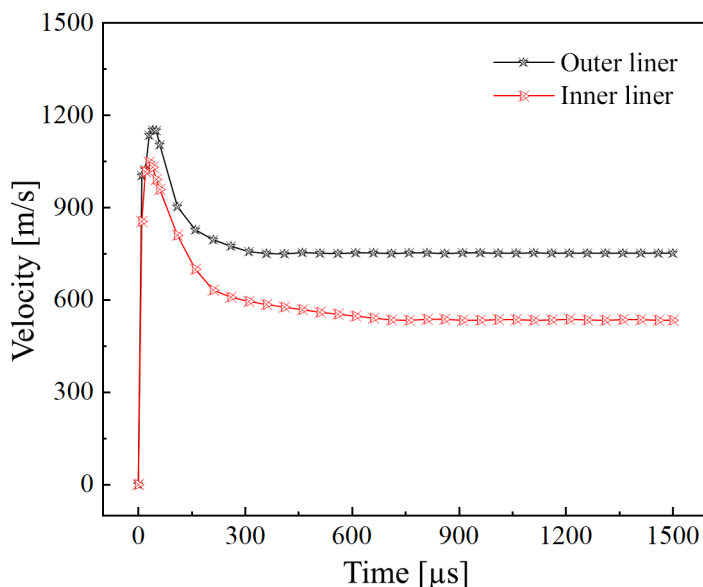
Figure 19. Flight velocity-time curves of the two projectiles of the CEFP

The penetration power of a CEFP is closely related to the flight velocity of the formed projectile. Figure 18 shows the velocity distribution field of the dynamic formation processes of a four-point initiated CEFP. In order to quantify the flight velocity of the front and rear projectiles, the flight velocity was tested. Figure 19 shows the flight velocity-time curve of the front and rear projectiles of a CEFP with tail wings formed by multi-point initiation. The numerical calculation results showed that the velocity of the explosively formed projectile presented a trend of "rising-falling-stabilizing" over time. In the time range of t = 0-20 μs, the flight velocities of the two projectiles both rose sharply under the loading effects of shock waves, and the inner and outer projectiles reached their maximum speeds of 1048 and 1151 m/s, respectively, which were very close to the results measured experimentally (shown in Figure 15). At this stage, the CEFP was in the preliminary forming stage, and the head and tail projectiles were not yet fully formed. Within t = 20-300 μs, the CEFP velocity had decreased slightly, and the head and tail projectiles of the CEFP have separated at this stage, and the flight velocity had decreased for the mutual collisions of the two projectiles in both radial and axial directions. After t = 300 μs, the CEFP has entered the free flight stage, and gradually formed two separated projectiles with stable flight velocities of 535 and 790 m/s, respectively. During the whole processes, the flight velocity of the inner projectile decreased more sharply than that of the outer liner, which

was mainly attributed to the kinetic energy transfer caused by the collisions between the inner and outer liners during the CEFP formation processes. Table 3 lists the experimental and simulation results of a CEFP with tail wings at the critical state of separation. The morphology, flight velocity and draw ratio of the CEFP were obtained by the high-speed images after binarization. As shown in Table 3, the morphology of the CEFP obtained by the high-speed camera was consistent with that obtained by simulation. The free flight velocity and draw ratio of the CEFP obtained by the high-speed camera were 810 m/s and 1.33, respectively, and were very close to the simulation results.

Table 3.   Comparison of experimental and simulation results of characteristic parameters of the CEFP

Method	CEFP shape	v [m/s]	l/d
High-speed image processing technology		810	1.33
Numerical simulation		790	1.37

5   Conclusions

♦ In the present study, a novel high-speed image processing technology for measuring the dynamic processes of CEFP formation was proposed, and the temperature field distribution and dynamic formation processes of a CEFP with tail wings were studied by the two-colour pyrometer technique, binary image processing method and contour detection algorithm, and the experimental results were verified using the LS-DYNA software.

♦ The results showed that multi-point initiation could form a CEFP with four symmetrical tail wings, the temperature of the detonation product during the explosion of the shaped charge was in the range of 2000-2600 K, and the pressure at the explosion center was 6.92 GPa. The formation processes of a CEFP could be divided into three phases, the impact phase, the propulsion phase and the free flight phase, and the free flight velocities of the inner and outer projectiles were 535 and 790 m/s, respectively. The free flight velocity and draw ratio of the projectile obtained from the high-speed image processing technology were 850 m/s and 1.33, respectively, which were in good agreement with the numerical simulation results.

References

[1] Rouge, P.; Weimann, K. Consequences on EFP Formation of an Intentionally Created Default. *Proc. 10th Int. Symp. on Ballistics*, San Antonio, USA, **1987**, 277-288.

[2] Bender, D.; Chhouk, B. Explosively Formed Penetrators (EFP) with Canted Fins. *Proc. 19th Int. Symp. on Ballistics,* Interlaken, Switzerland, **2001**, 755-762.

[3] Cayzac, R.; Roxan, E.; Alziary de Roquefort, T.; Renard, F.X.; Roux, D.; Balbo, P.; Patry, J.N. Computational Fluid Dynamics and Experimental Validations of the Direct Coupling Between Interior, Intermediate and Exterior Ballistics Using the Euler Equations. *J. Appl. Mech.* **2021**, *78*(6): paper 061006.

[4] Kagankiewicz, F.; Magier, M. Experimental Verification of the Internal Ballistics Numerical Simulations of Classical Weapons in Lagrangian Coordinates. *Continuum. Mech. Therm.* **2023**, *36*: 1323-1337.

[5] Yin, J.P.; Liu, Y.K.; Wang, Z.J.; Zhang, X.P.; Zhi, J.Z.; Zhang, Y.N. Formation and Penetration of PELE/EFP multi-Mode Warhead Based on Double-Layer Shaped Charge. *J. Energ. Mater.* **2023**, *41*(1): 4-26.

[6] Elshenawy, T.; Li, Q.M.; Elbeih, A. Experimental and Numerical Investigation of Zirconium Jet Performance with Different Liner Shapes Design. *Def. Technol.* **2022**, *18*(1): 12-26.

[7] Wang, X.; Jiang, J.W.; Sun, S.J.; Men, J.B.; Wang, S.Y. Investigation on the Spatial Distribution Characteristics of behind-Armor Debris Formed by the Perforation of EFP through Steel Target. *Def. Technol.* **2020**, *16*(1): 119-135.

[8] Zu, X.D.; Huang, Z.X.; Zhu, C.S.; Xiao, Q.Q. Study of Detonation Wave Contours in EFP Warhead. *Def. Technol.* **2016**, *12*(2): 129-133.

[9] Li, R.; Li, W.B.; Wang, X.M.; Li, W.B. Effects of Control Parameters of three-Point Initiation on the Formation of an Explosively Formed Projectile with Fins. *Shock Waves* **2018**, *28*: 191-204.

[10] Weimann, K. Research and Development in the Area of Explosively Formed Projectiles Charge Technology. *Propellants Explos., Pyrotech.* **1993**, *18*(5): 294-298.

[11] Liu, J.Q.; Gu, W.B.; Lu, M.; Xu, H.M.; Wu, S.Z. Formation of Explosively Formed Penetrator with Fins and Its Flight Characteristics. *Def. Technol.* **2014**, *10*(2): 119-123.

[12] Li, W.B.; Wang, X.M.; Li. W.B. The Effect of Annular multi-Point Initiation on the Formation and Penetration of an Explosively Formed Penetrator. *Int. J. Impact. Eng.* **2010**, *37*(4): 414-424.

[13] Li, Y.B.; Wang, J.X.; Liu, Z.T.; Tang, K.; Wang, H.F.; Cheng, X.W. Orthogonal Optimization Design and Experiments on Explosively Formed Projectiles with Fins. *Int. J. Impact. Eng.* **2023**, *173*: paper 104462.

[14] Liu, J.; Chen, X.; Du, Z.H. A Study on the Surface Overpressure Distribution and Formation of a Double Curvature Liner under a two-Point Initiation. *Def. Technol.* **2023**, *18*(1): 148-157.

[15] Ma, H.B.; Zheng, Y.F.; Wang, H.F.; Ge, C.; Su, C.H. Formation and Impact-induced Separation of Tandem EFPs. *Def. Technol.* **2020**, *16*(3): 668-677.

[16] Hu, F.F.; Cheng, Y.F.; Zhang, B.B.; Jiang, B.Y.; Ji, C.; Liu, R. Flame Propagation and Temperature Distribution Characteristics of Magnesium Dust Clouds in an Open Space. *Powder Technol.* **2022**, *404*: paper 117513.

[16] Cheng, Y.F.; Yao, Y.L.; Wang, Z.H.; Zhang, B.B.; Xia, Y.; Liu, R.; Shu, C.M. An Improved two-Colour Pyrometer Based Method for Measuring Dynamic Temperature Mapping of Hydrogen-Air Combustion. *Int. J. Hydrogen Energy* **2021**, *46*(69): 34463-34468.

[17] Jang, J.S.; Oh, S.H.; Roh, T.S. Development of three-Dimensional Numerical Model for Combustion-flow in Interior Ballistics. *J. Mech. Sci. Technol.* **2016**, *30*: 1631-1637.

[18] Brandeis, D.J. Effect of Shape and Asymmetry on the Aerodynamic Performance of Explosively Formed Projectiles. *Proc. 13th Int. Symp. on Ballistics,* Stockholm, Sweden, **1992**, 137-144.

[19] Yang, Y.; Wei, C.; Chen, Z.P.; Yao, Y.K.; Chen, X.; Jia, Y.S.; Li, W.; Hu, J.N. Multi-dimensional Numerical Simulation and Experimental Investigation of Monel Alloy/ Cu Explosive Cladded Rod. *J. Mater. Sci.* **2022**, *57*: 21363-21377.

[20] Zhang, K.; Zhao, C.X.; Ji, C.; Zhang, S.; Wang, X.; Jiang, T.; Wu, G. Numerical Simulation and Experimental Study of the Damage Law of EFP Warhead Charging of Cylindrical Shells Under Different Angles. *Lat. Am. J. Solids. Stru.* **2022**, *19*: paper e451.

[21] Jang, J.S.; Sung, H.G.; Roh, T.S.; Choi, D.W. Numerical Analysis of Interior Ballistics through Eulerian-Lagrangian Approach. *J. Mech. Sci. Technol.* **2013**, *27*: 2351-2357.

[22] Berner, C.; Fleck, V. Pleat and Asymmetry Effects on the Aerodynamics of Explosively Formed Penetrators. *Proc. 18th Int. Symp. on Ballistics,* San Antonio, USA, **1999**, 237-245.

[23] Izarra, C.D.; Gitton, J.M. Calibration and Temperature Profile of a Tungsten Filament Lamp. *Eur. J. Phys*. **2010**, *31*(4): 933-942.

[24] Yao, Y.L.; Cheng, Y.F.; Zhang, Q.W.; Xia, Y.; Hu, F.F.; Wang, Q.; Chen, Y. Explosion Temperature Mapping of Emulsion Explosives Containing TiH_2 Powders with the two-Color Pyrometer Technique. *Def. Technol.* **2022**, *18*(10): 1834-1841.

[25] Jiang, F.; Wang, X.F.; Huang, Y.F.; Feng, B.; Tian, X.; Niu, Y.L.; Zhang, K. Effect of Particle Gradation of Aluminum on the Explosion Field Pressure and Temperature of RDX-based Explosives in Vacuum and Air Atmosphere. *Def. Technol.* **2019**, *15*(6): 844-852.

Contribution

Chang-Xiao Zhao: foundations

Yangfan Cheng: conception, foundations, methods, performing the experimental part, performing the statistical analysis, other contributions to the publication

Dan-Yi Li: performing the experimental part

Bei-Bei Zhang: performing the experimental part

Xin Wang: performing the statistical analysis

Chong Ji: performing the statistical analysis, other contributions to the publication